FULL PAPER

Open Access

Solar and lunar daily geomagnetic variations and their equivalent current systems observed by Swarm

Yosuke Yamazaki*

Abstract

This paper describes solar and lunar daily variations of the geomagnetic field over low- and mid-latitude regions, using vector magnetometer data from Swarm satellites at altitudes of ∼500 km during the solar minimum years of 2017–2020. The average solar variation of the geomagnetic field is within the range of ±14 nT, while the lunar variation is within ±2 nT. The latter is comparable to the ocean tidal field. A spherical harmonic analysis is performed on the solar and lunar variations to evaluate their internal and external equivalent current systems. The results show that both the solar and lunar variations are mainly of internal origin, which can be attributed to combined effects of ionospheric dynamo currents and induced underground currents. Global patterns of the internal solar and lunar current systems are consistent with the corresponding external current systems previously reported based on ground observations. The Swarm external currents are mainly in the meridional direction, and are likely associated with interhemispheric field-aligned currents. Both the internal and external current systems depend on the season and longitude.

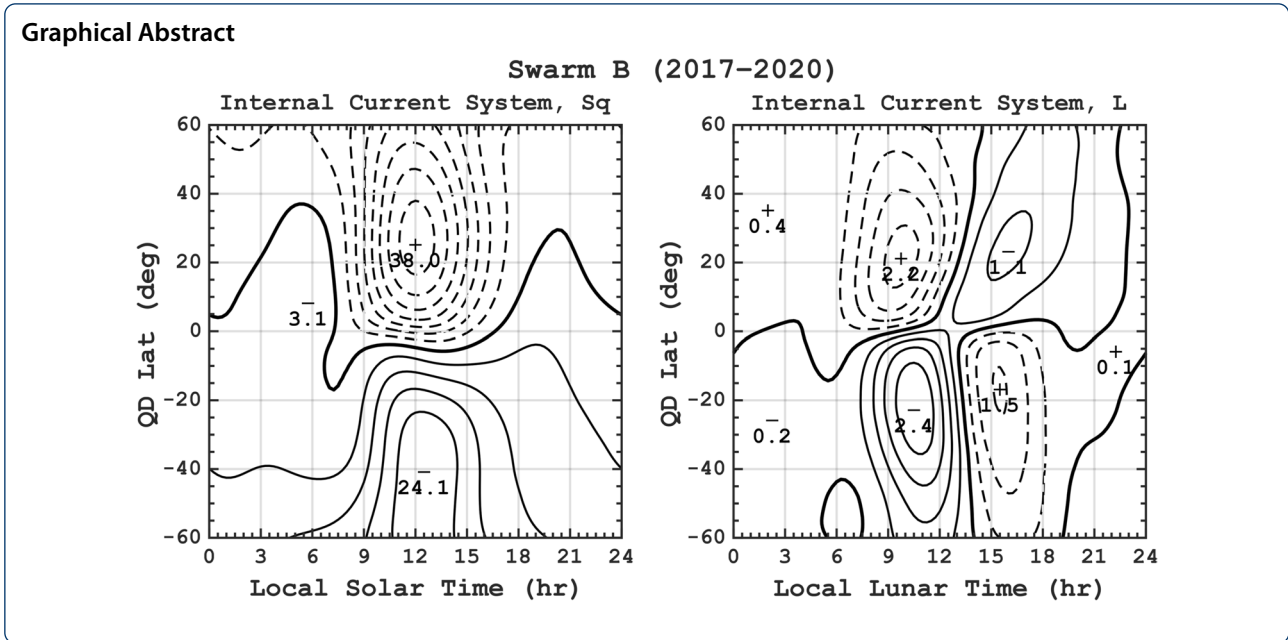**Keywords:** Geomagnetic field, Sq, L, Daily variation, Ionospheric currents, Swarm

*Correspondence: yamazaki@iap-kborn.de

Leibniz Institute of Atmospheric Physics (IAP), Schloßstraße 6,
18225 Kühlungsborn, Germany

Graphical Abstract

Introduction

The Earth's upper atmosphere is weakly ionized, as it receives energy inputs from the Sun in the form of electromagnetic waves. Ionized particles interact with neutrals by collisions and move through the ambient geomagnetic field, which gives rise to an electromotive force to support electric fields and currents. The process is known as the ionospheric wind dynamo, or simply ionospheric dynamo, and it is the dominant production mechanism of ionospheric electric fields and currents at middle and low latitudes during geomagnetically quiet periods (e.g., Richmond 1995a; Heelis 2004). The dynamo currents flow mainly on the dayside at E-region altitudes (ca 90–150 km), where the electrical conductivity of the ionosphere is greatest. At night, the ionospheric conductivity is smaller by about two orders of magnitude (e.g., Richmond 2011). Thus, the currents are also much weaker and have a negligible effect on the geomagnetic field on the ground. The daytime presence and nighttime absence of the magnetic effect associated with ionospheric dynamo currents lead to daily variation of the geomagnetic field measured at ground stations. Geomagnetic daily variation is smooth and regular in appearance on geomagnetically quiet days when high-frequency geomagnetic disturbances associated with geomagnetic storms and substorms are absent, and is often referred to as solar-quiet (Sq) variation (e.g., Campbell 1989; Yamazaki and Maute 2017).

A spherical harmonic analysis is a technique that is most commonly used to estimate the ionospheric current system from Sq. The Sq field is expressed in terms of a magnetic scalar potential, which is a solution to the Laplace's equation. That is

$$M(r,\theta,\phi) = M_{\mathrm{ex}}(r,\theta,\phi) + M_{\mathrm{in}}(r,\theta,\phi) \tag{1}$$

$$M_{\mathrm{ex}} = R\sum_{n=1}^{\infty}\left[\left(\frac{r}{R}\right)^n \sum_{m=0}^{n}\left\{g_{\mathrm{ex}}{}_n^m \cos(m\phi) + h_{\mathrm{ex}}{}_n^m \sin(m\phi)\right\}P_n^m(\cos\theta)\right] + C_{\mathrm{ex}} \tag{2}$$

$$M_{\mathrm{in}} = R\sum_{n=1}^{\infty}\left[\left(\frac{R}{r}\right)^{n+1} \sum_{m=0}^{n}\left\{g_{\mathrm{in}}{}_n^m \cos(m\phi) + h_{\mathrm{in}}{}_n^m \sin(m\phi)\right\}P_n^m(\cos\theta)\right] + C_{\mathrm{in}}, \tag{3}$$

where M is the magnetic scalar potential for Sq. r, θ and ϕ are the radial distance (in km), colatitude (in rad) and longitude (in rad), respectively. M_{ex} and M_{in} are external and internal parts of the magnetic scalar potential, respectively. C_{ex} and C_{in} are constant terms. R is a reference height (in km), which would be the Earth's radius R_E for the analysis of ground magnetic data. $P_n^m(\cos\theta)$ are Schmidt quasi-normalized associated Legendre functions. The integers n and m are degree and order, respectively. g_n^m and h_n^m are the so-called Gauss coefficients, with subscripts "ex" and "in" representing external and internal components, respectively. Using M, magnetic perturbations in the northward (X), eastward (Y) and vertical (Z) components can be expressed as follows:

$$B_X = \frac{1}{r}\frac{\partial M}{\partial \theta} \tag{4}$$

$$B_Y = -\frac{1}{r\sin\theta}\frac{\partial M}{\partial \phi} \tag{5}$$

$$B_Z = \frac{\partial M}{\partial r}. \tag{6}$$

The Gauss coefficients can be determined so that the deviation of B_X, B_Y and B_Z from the observed Sq field in the X, Y and Z components will be minimized. Substituting the Gauss coefficients to (1)–(3), the external (M_{ex}) and internal (M_{in}) components of the magnetic scalar potential can be separately obtained. In (2), M_{ex} increases with increasing r, thus representing the source above the surface. On the other hand, M_{in} in (3) increases with decreasing r, and thus the source exists below the surface. The biggest advantage of the spherical harmonic analysis is the mathematical separation of external and internal sources.

The ionospheric currents associated with Sq are often expressed in terms of equivalent current system. An equivalent current system is a hypothetical electric current system on a spherical plane that would produce the same magnetic variations as those observed. It is a mathematically compact, two-dimensional, representation of the true ionospheric current system that has a three-dimensional structure (e.g., Pfaff et al. 2020). Using the Gauss coefficients, external and internal equivalent current systems can be derived as follows:

Here, J_{ex} and J_{in} are the external and internal components of the equivalent current function (in amperes). The constant terms C'_{ex} and C'_{in} may be determined so that equivalent currents will be small at night. Numerous studies have examined external and internal equivalent current systems for Sq variations observed on the ground (e.g., Chapman and Bartels 1940; Matsushita and Maeda 1965a; Campbell and Schiffmacher 1985, 1988; Haines and Torta 1994; Takeda 1999, 2002; Yamazaki et al. 2011; Stening and Winch 2013; Çelik 2013; Owolabi et al. 2022). The external current system for Sq usually shows two large current vortices on the dayside, directed counterclockwise in the northern hemisphere and clockwise in the southern hemisphere. The internal current system for Sq also shows two dayside current vortices, but the currents are weaker and in the opposite direction, that is, clockwise in the northern hemisphere and counterclockwise in the southern hemisphere. In general, the external Sq current system is attributed to ionospheric dynamo currents, and the internal current system is ascribed to secondary currents flowing in the conductive Earth induced by the primary ionospheric currents (e.g., Kuvshinov et al. 2007).

Numerical studies (e.g., Richmond et al. 1976; Forbes and Lindzen 1976; Takeda and Maeda 1980) have shown that solar tidal winds at E-region heights (10–10^2 m/s velocity) can drive sufficiently strong ionospheric currents (1–10 μA/m^2) to explain Sq variation on the ground (10–10^2 nT). The main cause of the solar tidal motion in the upper atmosphere is in-situ heating due to the absorption of extreme ultraviolet solar radiation by O, O_2 and N_2 on the dayside (Hagan et al. 2001). In addition to the locally generated tides in the upper atmosphere, upward-propagating tides originating from the troposphere and stratosphere also make contributions to the ionospheric dynamo (Richmond and Roble 1987; Yamazaki et al. 2014). The upward-propagating tides from the lower atmosphere contain not only solar tides but also lunar tides, which are excited by the gravitational force of the Moon (Lindzen and Chapman 1969). The semidiurnal lunar tide, M_2, is the dominant mode of the atmospheric lunar tide at heights of the E region (Vial and Forbes 1994; Pedatella et al. 2012a; Zhang and

$$J_{ex} = R\sum_{n=1}^{\infty}\left[-\frac{10}{4\pi}\frac{2n+1}{n+1}\left(\frac{r}{R}\right)^n\sum_{m=0}^{n}\left\{g_{ex}{}_n^m\cos(m\phi)+h_{ex}{}_n^m\sin(m\phi)\right\}P_n^m(\cos\theta)\right]+C'_{ex} \tag{7}$$

$$J_{in} = R\sum_{n=1}^{\infty}\left[\frac{10}{4\pi}\frac{2n+1}{n}\left(\frac{R}{r}\right)^{n+1}\sum_{m=0}^{n}\left\{g_{in}{}_n^m\cos(m\phi)+h_{in}{}_n^m\sin(m\phi)\right\}P_n^m(\cos\theta)\right]+C'_{in}. \tag{8}$$

Forbes 2013). The modulation of the ionospheric dynamo by M_2 leads to lunar daily variation of the geomagnetic field, which is denoted as L (e.g., Tarpley 1970; Rastogi and Trivedi 1970; Stening and Winch 1979).

L depends not only on the phase of the Moon but also on local solar time. This is because the dynamo currents driven by M_2 are subject to the diurnal modulation of the ionospheric conductivity, which is controlled by local solar time. The most commonly used form to express L is as follows (e.g., Chapman and Bartels 1940):

$$L(t, \nu) = \sum_{k=1}^{4} l_k \sin{(kt - 2\nu + \epsilon_n)}. \tag{9}$$

Here, t is the local solar time. ν is the lunar phase; $\nu = 0$ (or 2π) corresponds to the new Moon and $\nu = \pi$ corresponds to the full moon (Sugiura and Fanselau 1966). l_k and ϵ_k are the amplitude and phase, respectively. L is generally much smaller in amplitude than Sq, and its main period (12.4 h) is very close to the semidiurnal (12.0 h) component of Sq. Thus, it is difficult to distinguish L from Sq on a daily basis. Nevertheless, L and Sq can be statistically separated using long-term data (e.g., Chapman and Miller 1940). Moreover, using the spherical harmonic analysis, one can separate external and internal equivalent current systems for L. Studies have shown that the equivalent current system for L typically has four current vortices on the dayside, with two vortices in the northern hemisphere and the other two in the southern hemisphere (e.g., Matsushita and Maeda 1965b; Matsushita 1968; Malin 1973; Matsushita and Xu 1984; Çelik 2014). This is different from the pattern of the Sq current system, which has one vortex in each hemisphere.

In the past two decades, attempts have been made to observe magnetic perturbations associated with Sq currents using satellite-borne magnetometer data. Turner et al. (2005, 2007) showed Sq variations in the total intensity of the geomagnetic field observed by CHAMP satellite (Reigber et al. 2002) during May–September 2001. Pedatella et al. (2011) used vector magnetometer data from the CHAMP satellite during 2006–2008, and showed that the equivalent Sq current system has two dayside current vortices, consistent with that derived from ground-based magnetometer data during the same period. Chulliat et al. (2016) combined vector magnetometer data from Swarm satellites (Friis-Christensen et al. 2006) and globally distributed ground stations during 2013–2015 to construct an empirical model of the Sq current system, which depends on latitude, longitude, time, and solar flux. Comprehensive Model (e.g., Sabaka et al. 2002, 2018), which is an empirical model of the geomagnetic field based on both ground and satellite data, also takes into account the Sq field.

The present study examines not only Sq but also L in vector magnetometer data from Swarm satellites. The spherical harmonic analysis will be performed on Sq and L at Swarm altitudes to evaluate their internal and external equivalent current systems. L current systems based on satellite data will be presented for the first time. It is noted that the meaning of external and internal equivalent current systems derived from Swarm magnetic data are different from those obtained from ground measurements. Since the Swarm satellites fly above the E region, the dynamo currents mainly contribute to the internal part of the Swarm Sq and L fields, while in the analysis of ground-based magnetometer data, the E-region dynamo currents mainly contribute to the external part. The discussion will be presented as to whether physically meaningful information can be obtained from Swarm external equivalent current systems.

Data processing

The main data employed in this study are vector magnetic field measurements from Swarm satellites. Swarm is ESA's satellite constellation mission launched in November 2013. The Swarm constellation consists of three identical satellites (Swarm A, B and C), which carry high-precision magnetometers (Leger et al. 2009), along with other scientific instruments for investigating the Earth's magnetic field and its sources (Friis-Christensen et al. 2008). The Swarm Level 1b magnetic product MAGX_LR_1B provides magnetic fields with a sampling rate of 1 Hz. Estimated uncertainties are also provided, which are typically less than 0.3 nT. For the present study, the magnetic field is expressed in the following three components: the center (C) component directed to the Earth's center, magnetic northward (N) component and magnetic eastward (E) component. The N and E components are derived by rotating the geographic northward and eastward components of the magnetic field using the magnetic declination given by the latest version of the International Geomagnetic Reference Field (Alken et al. 2021). Also, magnetic latitude and longitude in quasi-dipole (QD) coordinates (Richmond 1995b; Emmert et al. 2010) are calculated at each measurement point. It is known that ionospheric currents are better organized in QD coordinates than in geographical coordinates (e.g., Laundal and Richmond 2017).

This study focuses on the period from the years 2017 to 2020, representing typical solar minimum conditions. The solar flux index $F_{10.7}$ (Tapping 2013) was below 100 solar flux unit ($=10^{-22}$ W·m^{-2} ·Hz^{-1}) most of the times, as indicated in the top panel of Fig. 1. Only the data during geomagnetically quiet times are used. The selection of the quiet-time data is based on the geomagnetic activity
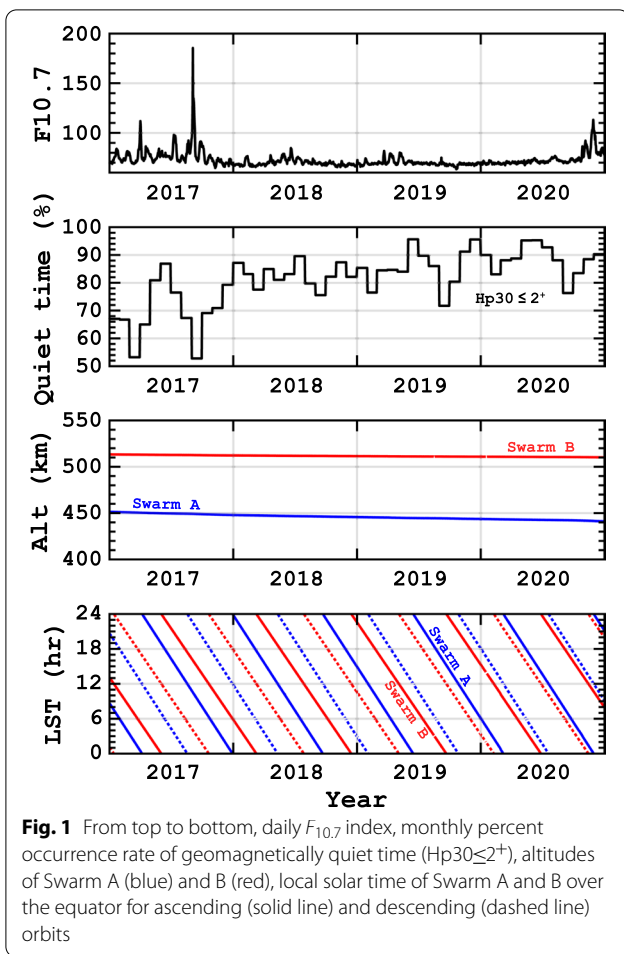
Fig. 1 From top to bottom, daily $F_{10.7}$ index, monthly percent occurrence rate of geomagnetically quiet time (Hp30≤2+), altitudes of Swarm A (blue) and B (red), local solar time of Swarm A and B over the equator for ascending (solid line) and descending (dashed line) orbits

index Hp30, which is similar to the Kp index (Matzka et al. 2021) but with higher temporal resolution of 30 min. Hp30 is available from the GFZ website at https://www.gfz-potsdam.de/hpo-index. The interested reader is referred to Yamazaki et al. (2022) for a detailed description of Hp30. The times with Hp30≤2+ are defined to be geomagnetically quiet. The second panel of Fig. 1 displays the monthly occurrence rate of Hp30≤2+. It shows that geomagnetic activity was particularly low during the years 2018–2020 when quiet periods account for more than 80% of the times for most months.

During the period considered, Swarm A and C flew side by side at an altitude of ~450 km, while Swarm B was flying separately at a higher altitude of ~510 km. The third panel of Fig. 1 shows the altitude of Swarm A and B. The magnetic data from Swarm C are used only when the data from Swarm A are unavailable. The combined data from Swarm A and C are referred to as Swarm A data, because the data from Swarm C account for less than 1% of the total data volume.

The bottom panel of Fig. 1 indicates the local solar time of Swarm A and B over the equator. The solid and dashed lines correspond to ascending and descending orbits, respectively, which are 12 h apart from each other. During 2017, the separation of Swarm A and B in local solar time was approximately 6 h, which achieves the best local solar time coverage by the two satellites. The difference in local solar time between Swarm A and B became smaller in the later years.

Satellite magnetic data contain contributions from various sources (e.g., Olsen and Stolle 2012). The main part (on the order of 10^4 nT) is generated by electric currents in the Earth's outer core, and referred to as "core field". It accounts for more than 95% of the total field intensity. Other contributions (10^0–10^2 nT) include not only the "ionospheric field" associated with Sq and L currents, but also the "crustal field" due to magnetized rocks in the solid Earth (e.g., Maus et al. 2006; Thébault et al. 2016), the "magnetospheric field" arising from large-scale magnetospheric currents (e.g., Lühr et al. 2017) and the "ocean tidal field" resulting from the tidal motion of electrically conductive ocean (e.g., Tyler et al. 2003; Grayver and Olsen 2019). These non-ionospheric fields need to be removed from the data before evaluating the ionospheric field (Stolle et al. 2016).

The CHAOS-7 geomagnetic field model (Finlay et al. 2020) is used to estimate the core, crustal and magnetospheric fields. The ocean tidal field is evaluated using the residuals between Swarm data collected from the nightside and corresponding CHAOS-7 predictions. The ocean dynamo operates equally on the dayside and nightside, while the ionospheric dynamo is ineffective on the nightside due to the small ionospheric conductivity (Malin 1970; Schnepf et al. 2014). Thus, using only the nightside data, the contamination from ionospheric L currents can be avoided. The nightside is defined here with the solar zenith angle $\chi > 105°$, under which the atmosphere from the surface to ~200 km is in the darkness. The M_2 ocean tidal field is determined by fitting the following formula to the quiet-time nightside data within each grid of $5° \times 5°$ in latitude and longitude:

$$L_o(\tau) = l_o \sin(2\tau + \epsilon_o). \qquad (10)$$

Here, τ is the lunar time ($= t - \nu$). l_o and ϵ_o are the amplitude and phase of the M_2 ocean tidal component, respectively. The N_2 and O_1 ocean tidal components are also known to be present in satellite magnetic data (e.g., Grayver and Olsen 2019), but they are ignored due to their small amplitudes. The M_2 ocean tidal field is evaluated separately for the N, E and C components and for the Swarm A and B data. The residual field, denoted here

as $\Delta\mathbf{B}$, is derived by subtracting the M_2 ocean tidal field described above from the Swarm-CHAOS residuals.

It is possible that $\Delta\mathbf{B}$ includes magnetic signatures of not only E-region currents but also F-region currents. It is known that neutral winds at F-region heights can locally drive dynamo currents (Rishbeth 1981; Maute and Richmond 2017) just like the ionospheric dynamo in the E region. Lühr and Maus (2006) observed magnetic perturbations of up to 5 nT associated with the F-region wind dynamo currents, mainly in the equatorial region, at altitudes of the CHAMP satellite (∼425 km) during August 2000–October 2004, near solar maximum. Park et al. (2010) demonstrated that the intensity of the F-region wind dynamo currents decreases with decreasing $F_{10.7}$. Based on the results presented by Park et al. (2010) and Lühr and Maus (2006), magnetic perturbations due to the F-region wind dynamo currents are estimated to be less than 1.5 nT during the solar minimum period considered in this study. It is noted that this would make only a marginal contribution to the Sq field that is examined in this paper.

Studies have also shown that satellite magnetometer data can be affected by F-region plasma gravity and pressure-gradient currents (Alken et al. 2017). These currents can also produce magnetic perturbations of up to 5 nT at satellite altitudes under solar maximum conditions (Lühr et al. 2003; Maus and Lühr 2006), but they are much weaker under solar minimum conditions due to the reduction of plasma density (Alken 2016). Their contributions to the Sq field is, thus, ignored in this paper.

Interhemispheric field-aligned currents (IHFACs) are another type of currents that are seen at satellite altitudes. The currents are generated by the north–south asymmetry of the E-region wind dynamo, and they flow along the magnetic field lines from one hemisphere to the other (e.g., van Sabben 1966; Fukushima 1979; Takeda 1990; Le Sager and Huang 2002). Although its current density is much smaller than that of the E-region dynamo currents, magnetic signatures of IHFACs are large enough to be sensed by satellite magnetometers (Olsen 1997; Yamashita and Iyemori 2002; Park et al. 2011). The part of IHFACs that flow across the spherical plane at the altitude of the satellite produces a non-potential field. Lühr et al. (2015) estimated IHFACs from the curl of the magnetic field observed by Swarm satellites. Such a non-potential field would make no contribution to equivalent current systems derived from the spherical harmonic analysis. Nevertheless, the part of IHFACs that is remote from the spherical plane of the satellite altitude might contaminate the equivalent current systems. This will be discussed in more detail later.

In the polar region, $\Delta\mathbf{B}$ would be dominated by the influence of region-1 and region-2 field-aligned currents and auroral electrojet (e.g., Laundal et al. 2018). It is assumed that the contamination of the Sq field by these currents can be ignored after the selection of geomagnetically quiet periods (Hp30≤2$^+$) and the exclusion of high-latitude data above 60° QD latitude. The equatorward boundary of the auroral oval depends on geomagnetic activity. Under geomagnetically quiet conditions, the boundary is generally above 60° magnetic latitude (e.g., Xiong et al. 2014).

The Sq and L fields at Swarm altitudes are evaluated using $\Delta\mathbf{B}$. The variation of Sq with local solar time is expressed as follows:

$$Sq(t) = \sum_{k=1}^{6} s_k \sin(kt - \delta_n), \tag{11}$$

where s_n and δ_n are the amplitude and phase. Solar harmonics from $k = 1$ to $k = 6$ are generally sufficient to represent Sq (e.g., Campbell 1990). At each magnetic latitude of 1° from 60°S to 60°N, Sq daily variation is determined by fitting the formula (11) to the data within ±0.75° magnetic latitudes. Similarly, L daily variation is determined at each magnetic latitude by fitting the formula (9). As can be seen in (9), L at a fixed value of the lunar phase ν depends only on local solar time t. In the remainder of the paper, the lunar phase corresponding to the new Moon ($\nu = 0$) is selected for presenting L, which facilitates the comparison of the results with many previous studies that also used $\nu = 0$ (e.g., Matsushita 1968).

Smooth distributions of both Sq and L fields are now obtained as a function of local solar time and magnetic latitude. The spherical harmonic analysis is performed on these smooth Sq and L fields based on (1)–(8), but replacing the colatitude θ and longitude ϕ with the magnetic colatitude and solar local time, respectively. In addition, N, E and C components of the geomagnetic field are used instead of X, Y and Z components. Equivalent current systems are evaluated at $r = R$ ($=R_E$), as both the altitude of the satellite and the distance of the source from the satellite are much smaller than the Earth's radius. The spherical harmonic expansion is truncated at the degree of $n = 40$, and at the order of $m = 6$ for Sq and $m = 4$ for L. $n = 40$ is found to be sufficient for resolving relatively small structures in the Sq and L fields near the magnetic equator associated with the equatorial electrojet (Chapman 1951). The equatorial electrojet is an enhanced zonal current flow along the dayside magnetic equator arising from a vertical electric field, which is localized within approximately ±3° from the magnetic equator (e.g., Stening 1995). Magnetic signatures of the equatorial electrojet can be found in satellite magnetometer data (Lühr et al. 2004; Alken and Maus 2007; Alken et al. 2015).

Like many previous studies based on ground observations (e.g., Matsushita and Maeda 1965a; Campbell et al. 1993), the spherical harmonic analysis is

performed in a grid of solar local time (i.e., geographical longitude) and magnetic latitude. The non-orthogonality of the grid is ignored. In addition, the difference between the direction of *N* (i.e., local magnetic north) and the direction of the northward unit vector of the QD coordinate system is ignored. Moreover, the difference between the direction of *E* (i.e., local magnetic east) and the direction of geographic east is ignored. These simplifications would lead to "assumption error" in the derived equivalent current function, which is difficult to evaluate. Meanwhile, "statistical error" was evaluated using the bootstrap technique (Efron 1981). The statistical error (one-sigma value) in the equivalent current function is generally below 0.1 kA, which is much smaller than the features discussed in this paper, and thus is ignored.

Results and discussion

Ocean tidal field

Figure 2 presents the amplitude (left panels) and phase (right panels) of the M_2 ocean tidal field obtained for Swarm A (panels a) and Swarm B (panels b). The amplitude is generally less than 2 nT in all components. The *C* component tends to be the largest among the three. There are regions, where the amplitude in the *C* component is enhanced, including the southern Indian Ocean, Tasman Sea, North Atlantic and Gulf of Alaska. The results are in good agreement with those presented in earlier studies (e.g., Saynisch-Wagner et al. 2021; Kuvshinov et al. 2021). The amplitudes in the *N* and *E* components are relatively large in the vicinity of the regions where the *C* component is large. The results are consistent between Swarm A and B in both amplitude and phase, demonstrating the robustness of the M_2 ocean tidal field.

Sq and L fields

Figure 3 shows the Sq field (panels a) and L field (panels b) in the *N* (left), *E* (middle) and *C* (right) components derived from the Swarm A data, including all seasons and universal times. In both (a) and (b), the upper panels show the observed Sq or L field, while the lower panels show the corresponding field reconstructed with a magnetic scalar potential; see (4)–(6). Thus, the difference between the upper and lower panels indicates the presence of non-potential fields. The difference is more evident in the *N* and *E* components than in the *C* component. This seems to suggest that the non-potential fields are mainly generated by electric currents in the radial direction. Field-aligned currents flowing across the satellite's orbital altitude (e.g., Lühr et al. 2015; Rodríguez-Zuluaga and Stolle 2019) may be considered as a possible

source. Besides, non-physical sources, including seasonal and UT biases as well as the assumption error mentioned earlier, could also contribute to the non-potential fields. However, identifying the causes of the non-potential fields is outside the scope of this study, thus no further analysis is performed on the non-potential fields.

The Sq field in Fig. 3a is within the range of ±14 nT. The largest variation is seen in the *N* component over the magnetic equator, where the E-region currents in the zonal direction are enhanced due to the equatorial electrojet. The Sq field in the *C* component shows a negative peak in the northern hemisphere and a positive peak in the southern hemisphere, reflecting the two-dayside-vortex pattern of the Sq current system in the E region.

The L field in Fig. 3b is within the range of ±2 nT. The magnitude is generally about one tenth of the Sq field, and is comparable with the M_2 ocean tidal field presented in Fig. 2. The L field in the *N* and *C* components shows semidiurnal variation, unlike Sq which mainly shows diurnal variation. The largest variation is in the *N* component near the magnetic equator due to the equatorial electrojet. The lunar daily variation of the equatorial electrojet was examined in detail by Yamazaki et al. (2017) based on Swarm and CHAMP data.

Figure 4 presents the same valuables as Fig. 3 except for the Swarm B data. The results are in agreement with those from Swarm A in terms of both pattern and magnitude of the Sq and L fields. The overall agreement between Swarm A and B results suggests that the obtained magnetic signatures associated with Sq and L are robust.

Equivalent current systems

Figure 5 depicts, from left to right, the Swarm internal equivalent current system for Sq, external equivalent current system for Sq, internal equivalent current system for L and external equivalent current system for L. The upper and lower panels show the results derived from the Swarm A and Swarm B data, respectively, including all seasons and universal times. For the Sq current systems, the equivalent currents of 5 kA flow between adjacent contour lines, while for the L current systems, the contour interval is 0.5 kA. The equivalent currents flow counterclockwise around positive peaks and clockwise around negative peaks.

The Swarm internal equivalent Sq current system shows a familiar pattern with a counterclockwise vortex in the northern hemisphere and a clockwise vortex in the southern hemisphere. The internal current system is contributed not only by E-region dynamo currents but also by induced underground currents. As mentioned, these
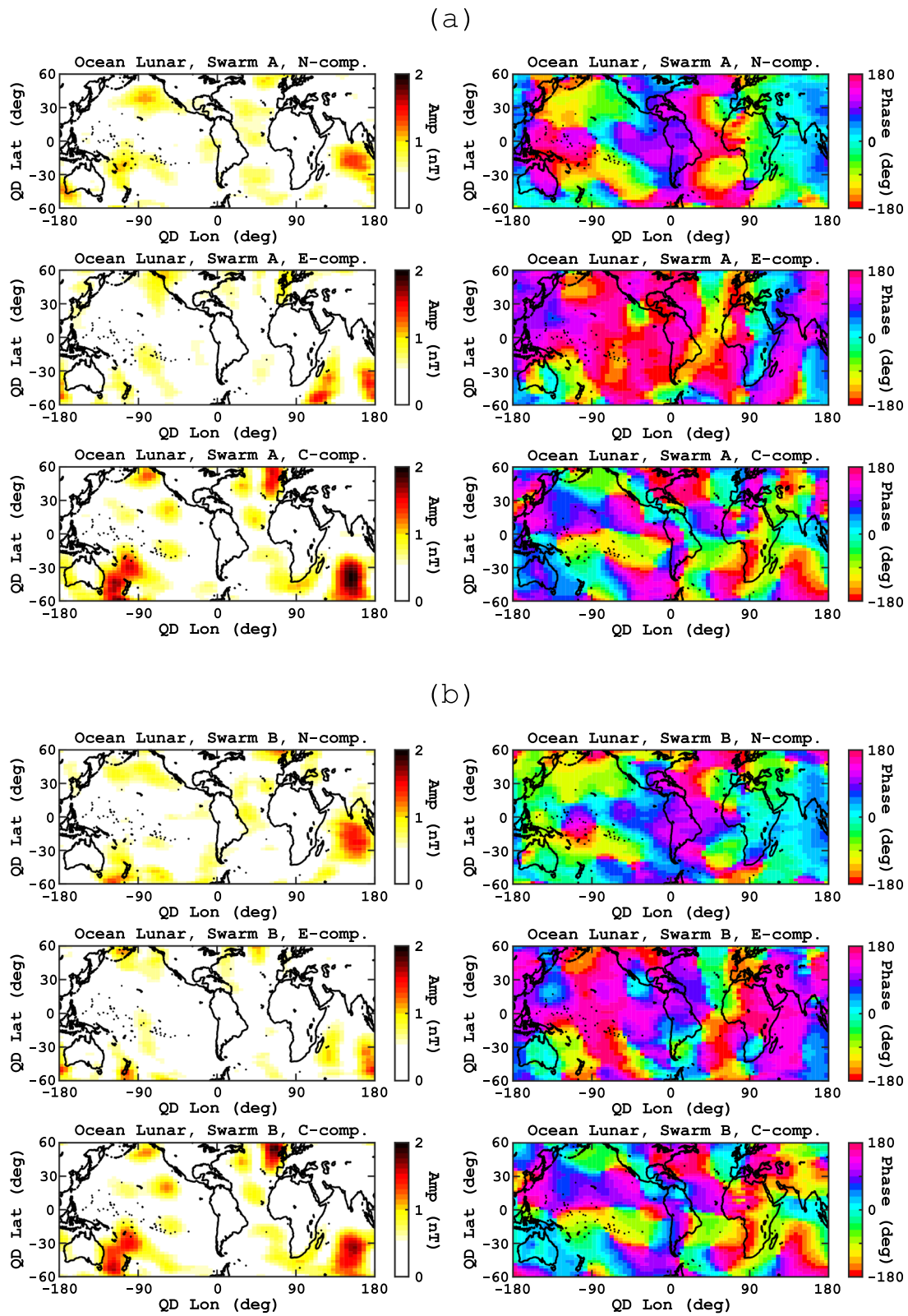
Fig. 2 Ocean tidal field for Swarm A (**a**) and B (**b**), as derived from quiet-time nightside data in the magnetic northward (*N*), magnetic eastward (*E*) and center (*C*) components during 2017–2020. Left panels show the amplitude, and right panels show the phase

two current systems are similar in pattern but they flow in opposite directions. According to previous studies, the intensity of the induced currents is approximately half that of the E-region currents (e.g., Campbell and Matsushita 1982; Campbell 1990). Thus, a rough estimate of the equivalent Sq current system in the E region can be obtained by multiplying the Swarm internal current function by a factor of two. This leads the peak value of the northern current vortex to be ~80 kA and the southern vortex to be ~50 kA. These values are comparable with those reported for the external current system from ground-based observations under solar minimum conditions (e.g., Campbell and Schiffmacher 1985, 1988; Yamazaki et al. 2011). The accurate separation of the E-region currents and induced underground currents requires the knowledge of the electrical conductivity distribution of the Earth and oceans (Koch and Kuvshinov 2013, 2015), and is beyond the scope of the present study.

The Swarm external equivalent Sq current system shows a single-vortex pattern with a negative peak around 13:00–14:00 local solar time near the magnetic equator. The pattern suggests northward and southward cross-equatorial currents in the noon sector and afternoon sector, respectively. It resembles the pattern of IHFACs, which are also in the northward direction in the noon sector and in the southward direction in the afternoon sector in an annual mean sense (e.g., Park et al. 2011).

The Swarm internal equivalent L current system for the new Moon ($\nu = 0$) has a counterclockwise vortex in the morning sector and a clockwise vortex in the afternoon sector in the northern hemisphere. In the southern hemisphere, a morning clockwise vortex and an afternoon counterclockwise vortex are seen in the Swarm B data, while in the Swarm A data, the afternoon counterclockwise vortex is not as clear. The overall pattern is consistent with that of the external equivalent L current system previously reported based on ground magnetic data (e.g., Matsushita 1968). This is the first time that the four-vortex pattern of the equivalent L current system is derived from satellite magnetometer data. The internal equivalent L current system contains contributions from both E-region dynamo currents and induced underground currents, such as the Swarm internal equivalent Sq current system. The external equivalent L current system does not show a clear pattern. As will be shown later,

this is not always the case depending on the season and longitude.

Seasonal dependence

Seasonal variations of the equivalent Sq and L current systems are examined. The residual data $\Delta \mathbf{B}$ from Swarm A and B are combined, and then separated into six bimonthly groups. The spherical harmonic analysis is performed on each group of the data to derive equivalent current systems. Figure 6a shows the seasonal variation of the Swarm internal equivalent current system for Sq. It is seen that the equivalent currents tend to be stronger in the summer hemisphere than in the winter hemisphere, which can be attributed to the enhancement of local ionospheric conductivity during summer (e.g., Wagner et al. 1980). The total currents that flow between the northern and southern Sq foci are largest during the equinox, which is mainly due to the seasonal change of solar tidal forcing (Yamazaki and Maute 2017).

The Swarm external Sq current system (Fig. 6b) also shows seasonal variation. Equivalent currents are particularly strong during the northern hemisphere summer (May–August). A negative peak of the current function is seen over the equatorial region in the afternoon sector between 12:00 and 15:00 local solar time and a weaker positive peak in the morning sector around 08:00 local solar time. The results suggest that equivalent currents flow across the magnetic equator from the southern hemisphere to the northern hemisphere around 12:00 local solar time, which are accompanied by weaker southward currents in the afternoon sector as well as in the morning sector. The pattern is somewhat similar during the equinoxes (Mar–April, September–October), when a negative peak is seen over the equatorial region in the afternoon sector between 12:00 and 15:00 local solar time. However, equivalent currents are much weaker than those during the norther hemisphere summer. During the northern hemisphere winter (November–February), a negative vortex appears in the morning sector between 09:00 and 12:00 local solar time. The dependence of the Swarm external Sq currents on local solar time and season is consistent with that of IHFACs. IHFACs are also strongest during the northern hemisphere summer, with northward currents around the noontime sector and weaker southward currents in the morning and afternoon sectors (e.g., Park et al. 2011, 2020a). The local solar

(See figure on next page.)
Fig. 3 Local solar time versus quasi-dipole (QD) latitude depiction of the Sq field (**a**) and L field at the new Moon (**b**), as derived from quiet-time data from Swarm A in the magnetic northward (*N*), magnetic eastward (*E*) and center (*C*) components during 2017–2020. In each of **a** and **b** the upper panels show the observed Sq or L field, while the lower panels show the Sq or L field reconstructed by a magnetic scalar potential described by (4)–(6). Contour steps are 2 nT for Sq and 0.4 nT for L. It is noted that local lunar time equals local solar time at the new Moon
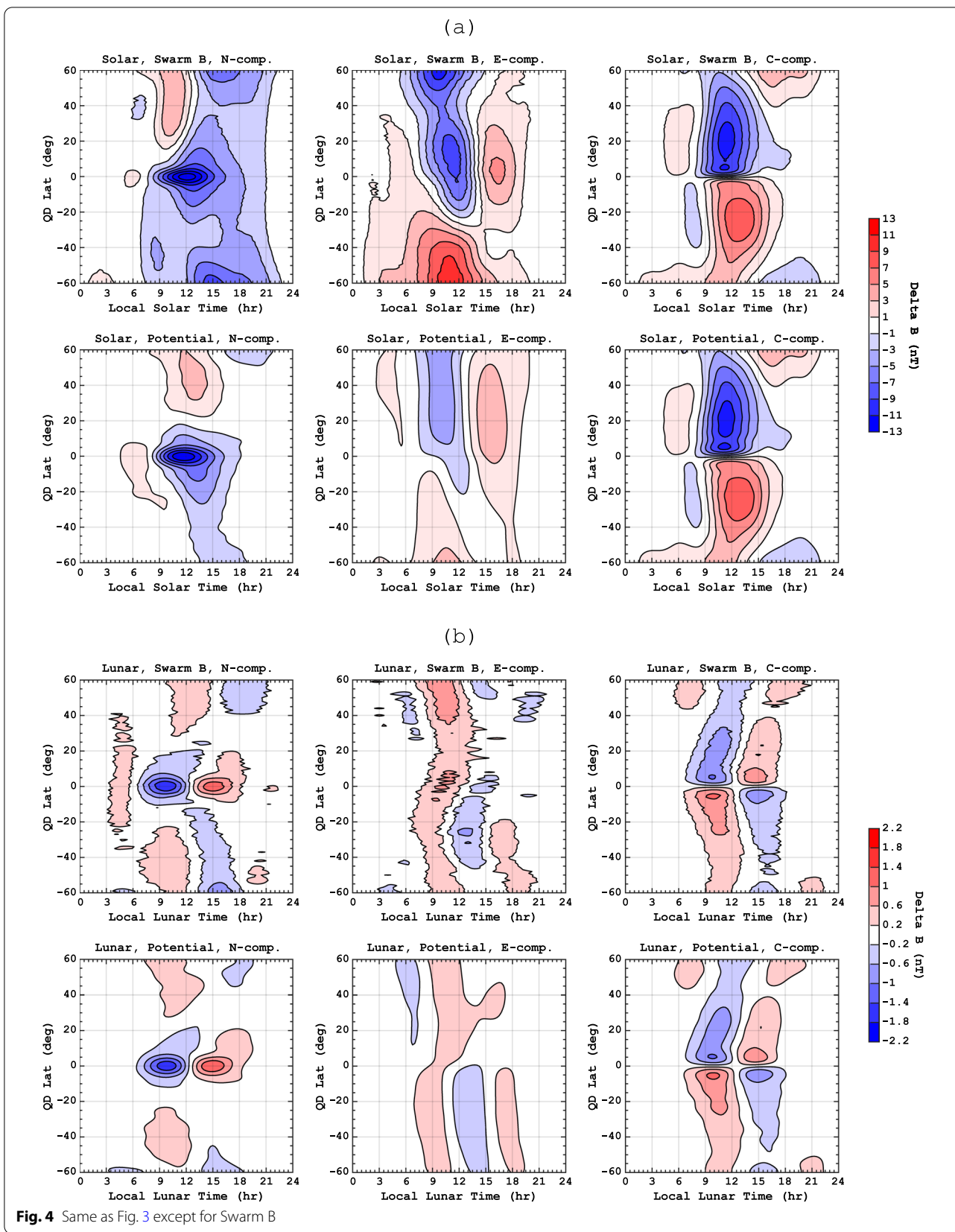
Fig. 3 (See legend on previous page.)
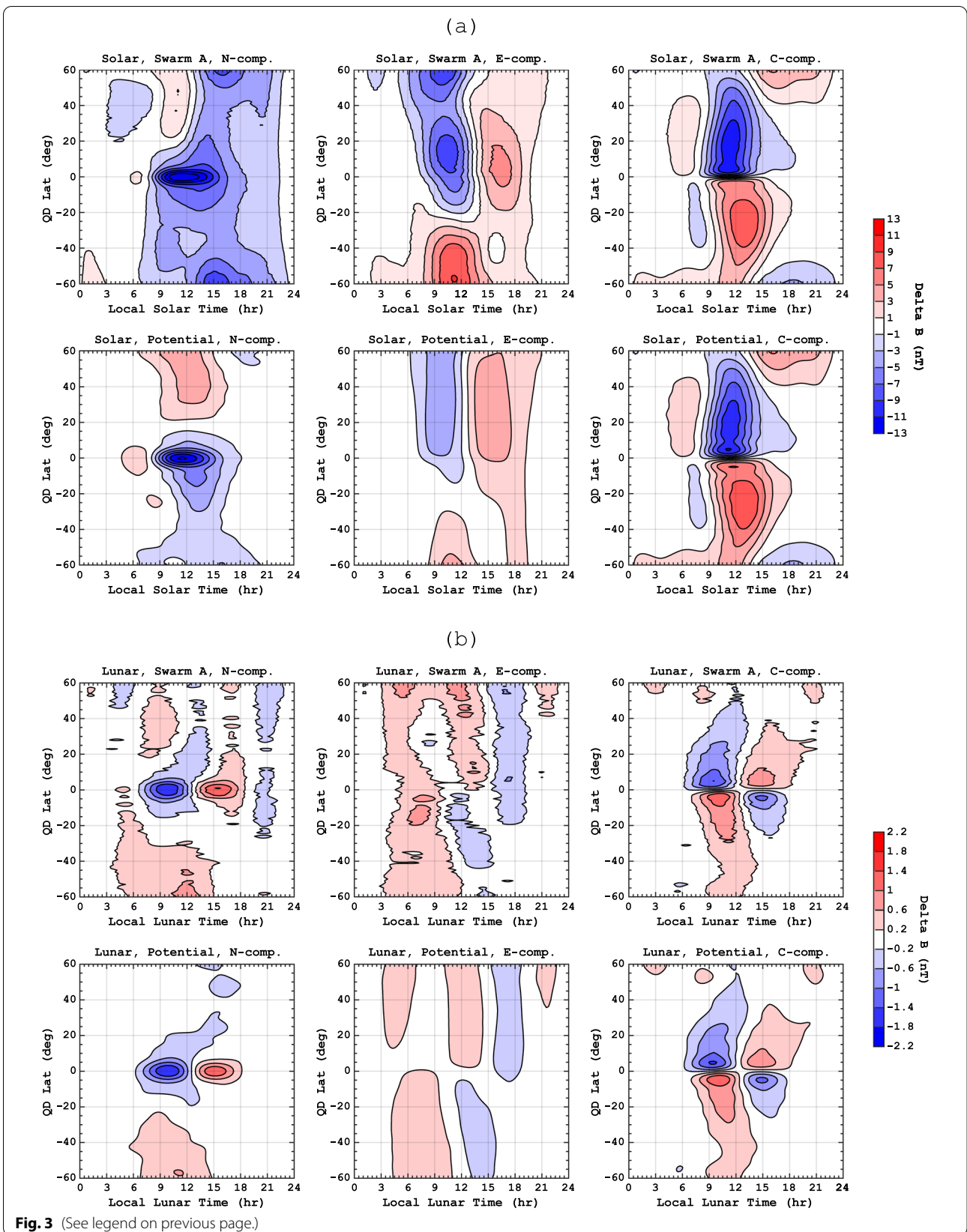
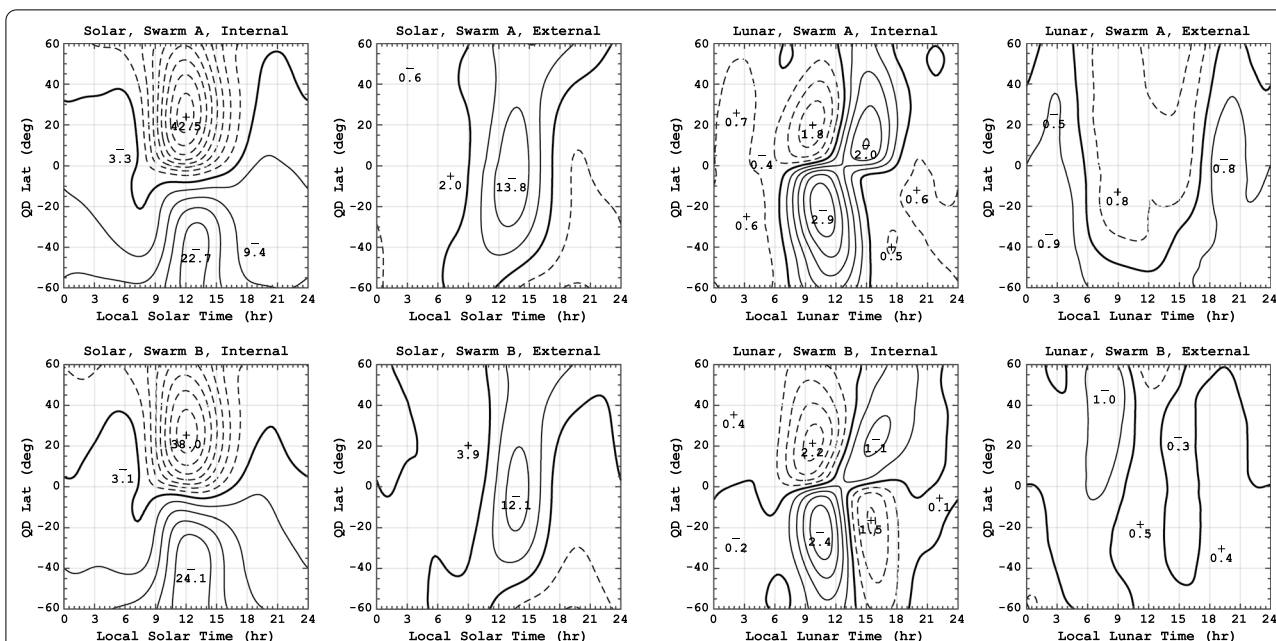**Fig. 4** Same as Fig. 3 except for Swarm B

Fig. 5 From left to right, Swam equivalent internal current system for Sq, external current system for Sq, internal current system for L and external current system for L, obtained using quiet-time data during 2017–2020 including all seasons and UTs. Upper and lower panels present the results derived with Swarm A and Swarm B data, respectively. Contour steps are 5 kA for Sq and 0.5 kA for L. It is noted that local lunar time equals local solar time at the new Moon

time pattern of IHFACs during the equinoxes is similar to that during the northern hemisphere summer but with reduced currents, and the pattern is unclear during the northern hemisphere winter (Park et al. 2020a). IHFACs do not strongly depend on solar activity (Park et al. 2011), so that their magnetic signatures can be detected during both solar maximum and solar minimum.

As mentioned earlier, satellite magnetometer data are contributed from various types of F-region currents, including F-region wind dynamo currents, plasma gravity and pressure-gradient currents. These currents are unlikely the main cause of the Swarm external Sq current system, as they are thought to be very weak under solar minimum conditions. Besides, the patterns of their equivalent current systems would be different from the Swarm external Sq current system, which shows cross-equatorial currents. The F-region wind dynamo currents flow in the meridional direction, but they are symmetric about the magnetic equator (Lühr and Maus 2006), which means that meridional currents flow into or out of the magnetic equator, rather than flowing across the magnetic equator. The plasma gravity and pressure-gradient currents flow mainly in the zonal direction (Alken et al. 2017).

Figure 7a depicts the seasonal variation of the Swarm internal L current system for $v = 0$. The L currents show annual variation with the maximum current intensity

during the northern hemisphere winter. For instance, the intensity of the currents that flow between the morning and afternoon foci is largest during January–February in both the northern hemisphere (5.6 kA) and southern hemisphere (6.3 kA), and smallest during July–August in both the northern hemisphere (4.2 kA) and southern hemisphere (2.1 kA). Previous studies have also noted that the L currents tend to be strongest during the northern hemisphere winter (e.g., Matsushita and Xu 1984). The annual variation of L can be attributed to that of lunar tidal forcing at E-region heights (e.g., Pedatella 2014). Besides, strong L currents during January–February may be contributed by enhanced lunar tides during sudden stratospheric warmings (SSW). SSW are large-scale dynamical disturbances in the Arctic middle atmosphere during the northern hemisphere winter (e.g., Baldwin et al. 2021). Studies have shown that the semidiurnal lunar M_2 tide can be amplified during SSW (e.g., Stening et al. 1997; Pedatella et al. 2012b; Zhang and Forbes 2014), which leads to an enhancement of L currents at mid and low latitudes (e.g., Fejer et al. 2010; Yamazaki 2014). Our data set covers major SSW in February 2018 (Rao et al. 2018) and January 2019 (Oberheide et al. 2020).

The seasonal variation of the Swarm external L current system for $v = 0$ is presented in Fig. 7b. The pattern of the current function is similar between May–June and
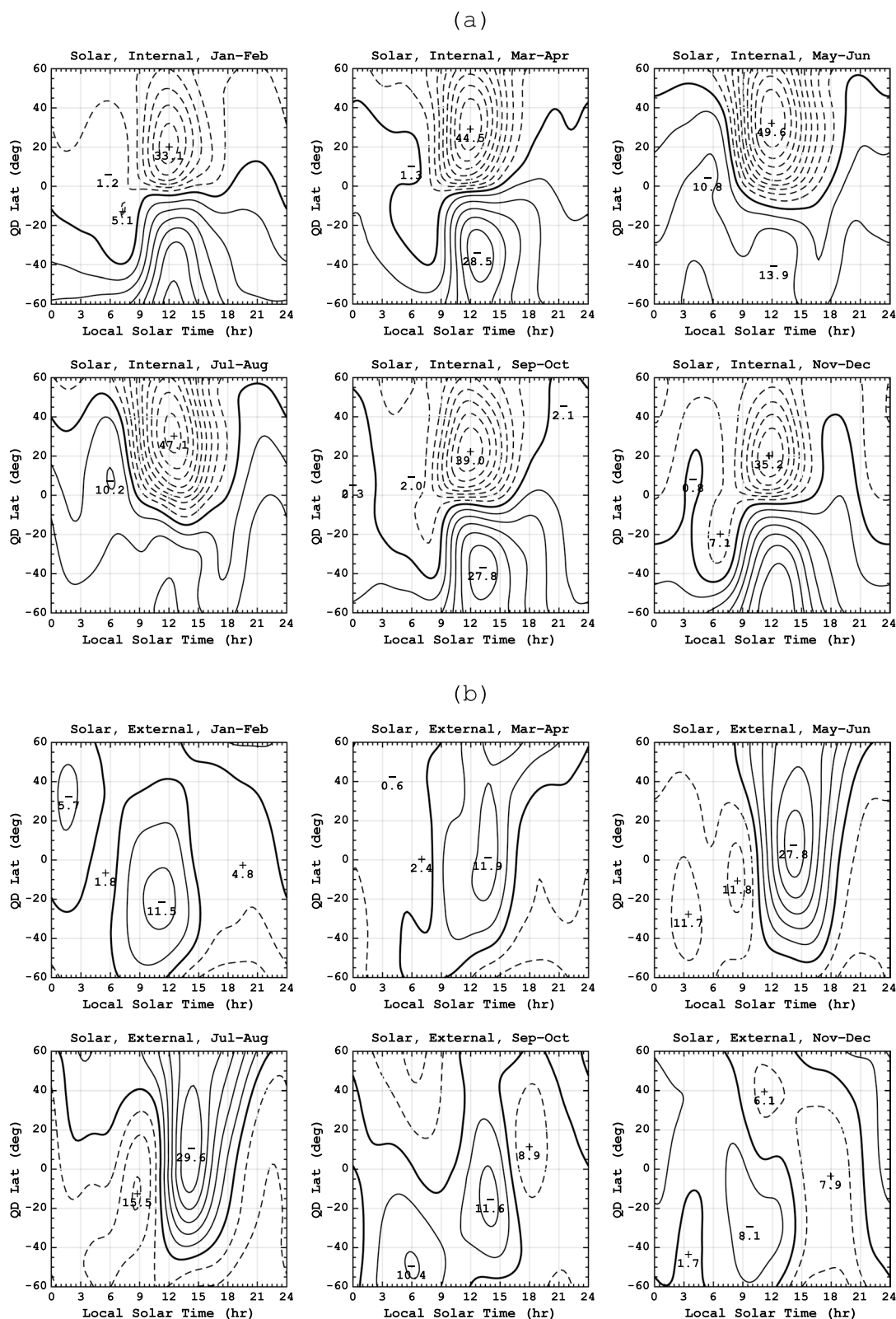
Fig. 6 Seasonal dependence of Swarm equivalent internal (**a**) and external (**b**) current systems for Sq, derived from quiet-time measurements by Swarm A and B during 2017–2020. Contour steps are 5 kA for both **a** and **b**
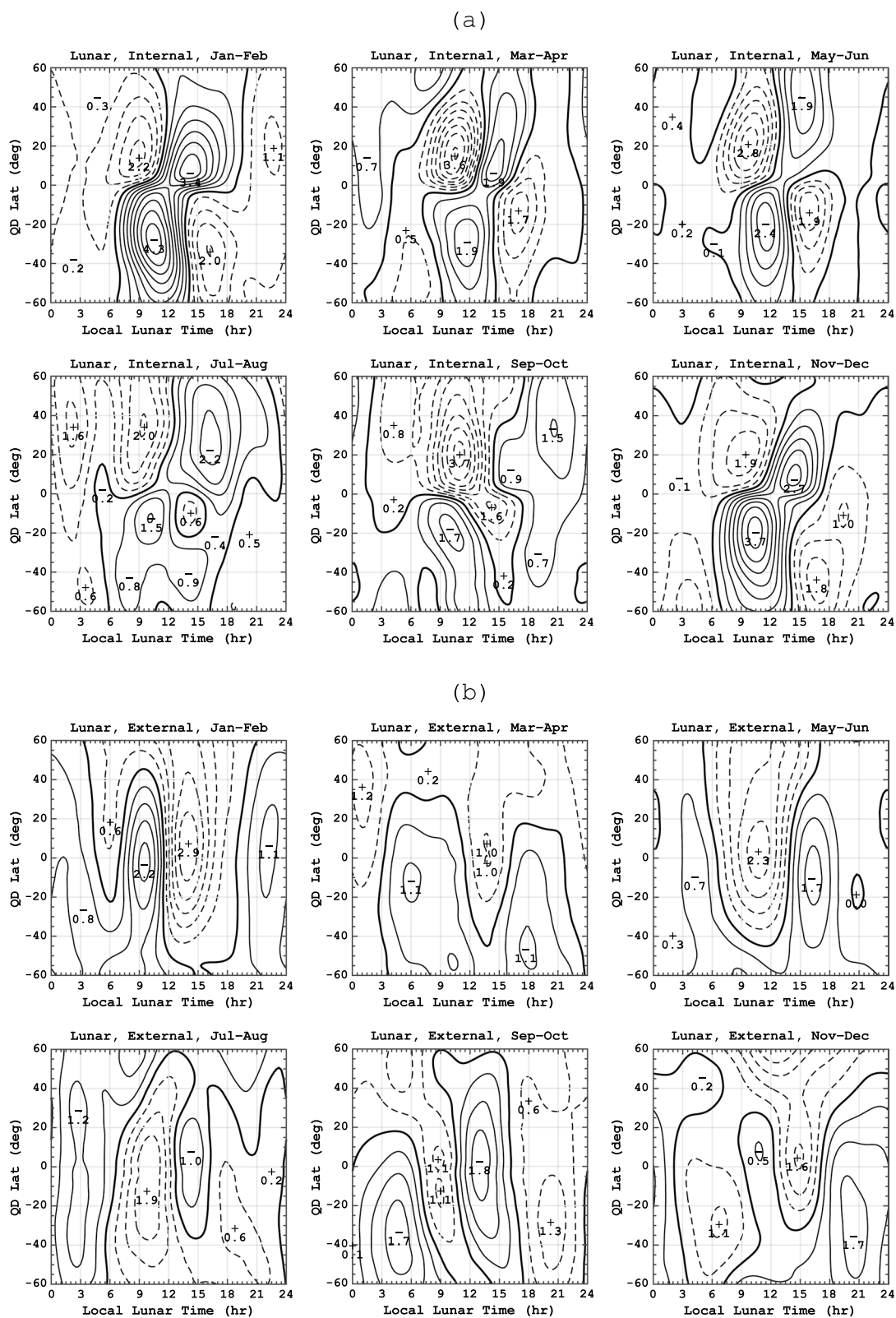
Fig. 7 Same as Fig. 6 except for L at the new Moon. Contour steps are 0.5 kA. It is noted that local lunar time equals local solar time at the new Moon

July–August, with a positive and negative peak over the equatorial region in the morning and afternoon sectors, respectively. The pattern is also similar between November–December and January–February, with a negative and positive peak in the morning and afternoon sectors, respectively. The direction of the equivalent currents during the northern hemisphere summer (May–August) is opposite of those during the northern hemisphere winter (November–February). Thus, the annual mean of the Swarm external L current system is small as shown in Fig. 5. During May–April, the pattern is more similar to those during the northern hemisphere winter than during the northern hemisphere summer. On the other hand, during September–October, the pattern is more similar to those during the northern hemisphere summer.

One possible explanation for the Swarm external L currents is the contribution of IHFACs. IHFACs are controlled by the ionospheric wind dynamo at E-region heights, and thus can be affected by the M_2 tide. Miyahara and Ooishi (1997) and Park et al. (2020a) numerically demonstrated that IHFACs are strongly influenced by tides and other large-scale waves coming from the middle and lower atmosphere. Lühr et al. (2019) pointed out that the intensity of IHFACs depends on the Moon phase. Yamazaki et al. (2020) demonstrated that the lunar variation of IHFACs is amplified during SSW. However, it is not well understood how the lunar variation of IHFACs depends on the season and local solar time. Future work is required to establish the seasonal climatology of the lunar variation of IHFACs, which then needs to be compared with the Swarm external L current system shown in Fig. 7b.

Longitude dependence

Sq and L fields depend not only on the season but also on longitude (e.g., Matsushita and Maeda 1965a; Stening and Winch 1979). The longitude dependence of Sq and L arises in part from the longitudinal dependence of the ionospheric conductivity, which itself depends on the plasma density and ambient geomagnetic field (Stening 1971). Besides, tidal winds (as seen at a fixed local solar or lunar time) vary with longitude (e.g., Forbes et al. 2008; Paulino et al. 2013), which would also contribute to the longitudinal dependence of Sq and L. To highlight the longitudinal dependence of Swarm equivalent Sq and L current systems, the data are separated into three groups

depending on the universal time, that is, 04:00–12:00 UT, 12:00–20:00 UT and 20:00–04:00 UT. According to Çelik (2013), the dayside Sq vortices are located in the Central Asian to Euro-African sector during 04:00–12:00 UT, in the American sector during 12:00–20:00 UT, and in the Pacific to Far Eastern sector during 20:00–04:00 UT. Moreover, each group of data is separated into two groups according to the season, that is, the northern hemisphere summer (April–September) and northern hemisphere winter (October–March).

Figure 8a presents the Swarm internal (upper panels) and external (lower panels) Sq current systems during the northern hemisphere summer months (April–September) in the Euro-African/Central Asian sector (left), American sector (middle) and Far Eastern/Pacific sector (right). It can be seen that the overall patterns of the current systems are similar at the three longitudinal sectors, with some differences in the current intensity. Figure 8b shows the same but for the northern hemisphere winter months (October–March). Besides the normal two-vortex pattern, the southern internal current system displays an additional counterclockwise vortex centered around 07:00 local solar time, which is most and least prominent in the Euro-African/Central Asian sector and in the Far Eastern/Pacific sector, respectively. The external current systems reveal cross-equatorial southward currents around 15:00 local solar time in the Euro-African/Central Asian sector and Far Eastern/Pacific sector, but not in the American sector. This might be related to the peculiarity of IHFACs over the American sector, which was noted by Park et al. (2020a, b).

Figure 9 is similar to Fig. 8 but for the Swarm L current systems. During the northern hemisphere summer months (April–September), the current patterns are consistent at different longitudinal sectors. That is, the internal current system has two vortices in each hemisphere, while the external current system has one counterclockwise vortex in the morning sector and one clockwise vortex in the afternoon sector over the equatorial region. During the northern hemisphere winter months (October–March), the internal current system shows the four-vortex pattern, but the counterclockwise vortex in the southern hemisphere is not as clear in the Euro-African/Central Asian sector as in the other longitude sectors. For the external current system, an afternoon counterclockwise vortex is seen in the Euro-African/Central Asian

(See figure on next page.)

Fig. 8 Swarm equivalent Sq current systems obtained from quiet-time magnetic observations by Swarm A and B during **a** the northern hemisphere summer (April–September) and **b** northern hemisphere winter (October–March) of 2017–2020. The results are presented for (left) 04:00–12:00 UT when the Euro-African/Central Asian sector is on the dayside, (middle) 12:00–20:00 UT when the American sector is on the dayside and (right) 20:00–04:00 UT when the Far Eastern/Pacific sector sector is on the dayside. In each of **a** and **b**, the upper panels show Swarm internal current systems, and the lower panels show Swarm external current systems. Contour steps are 5 kA
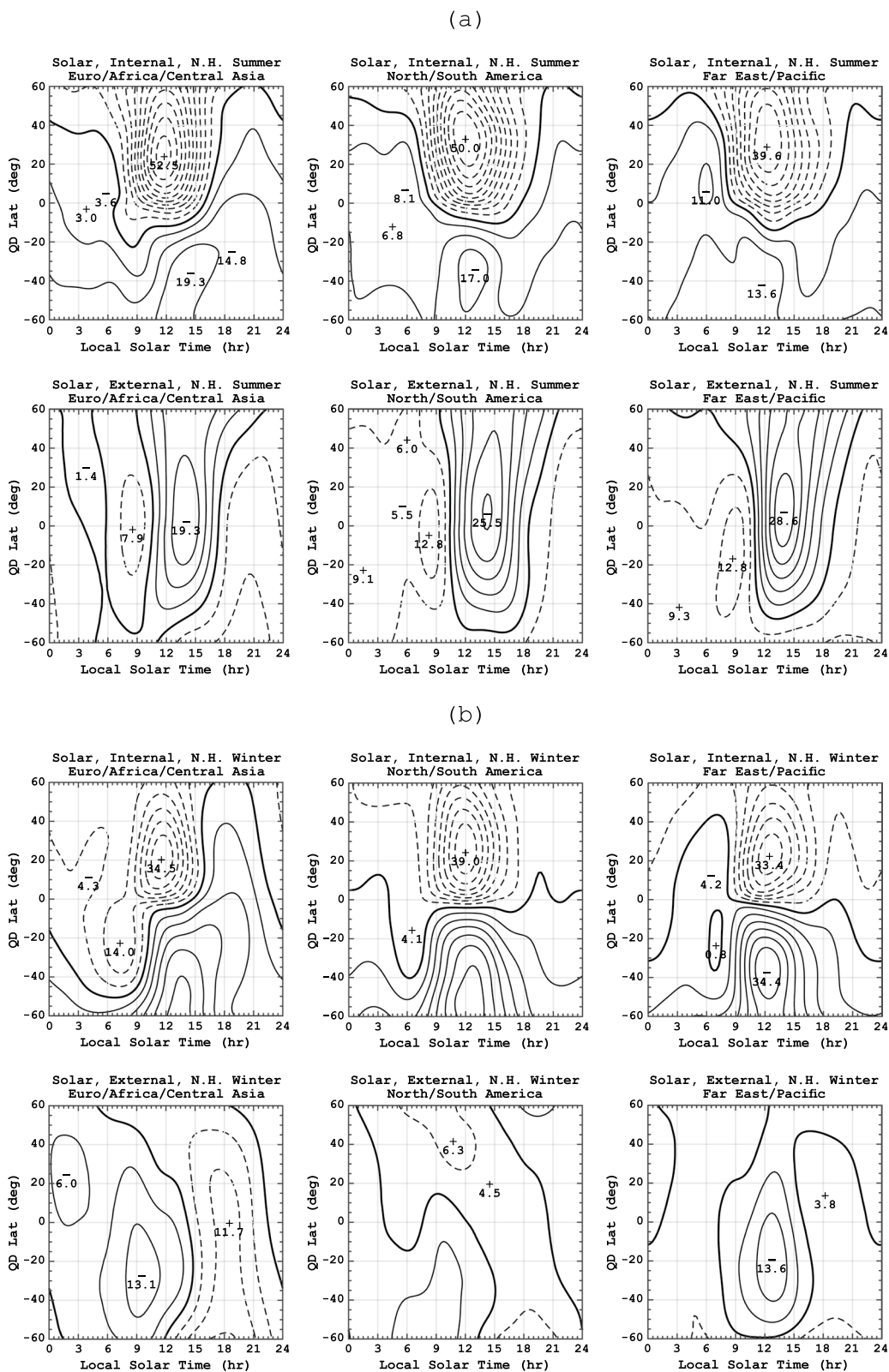
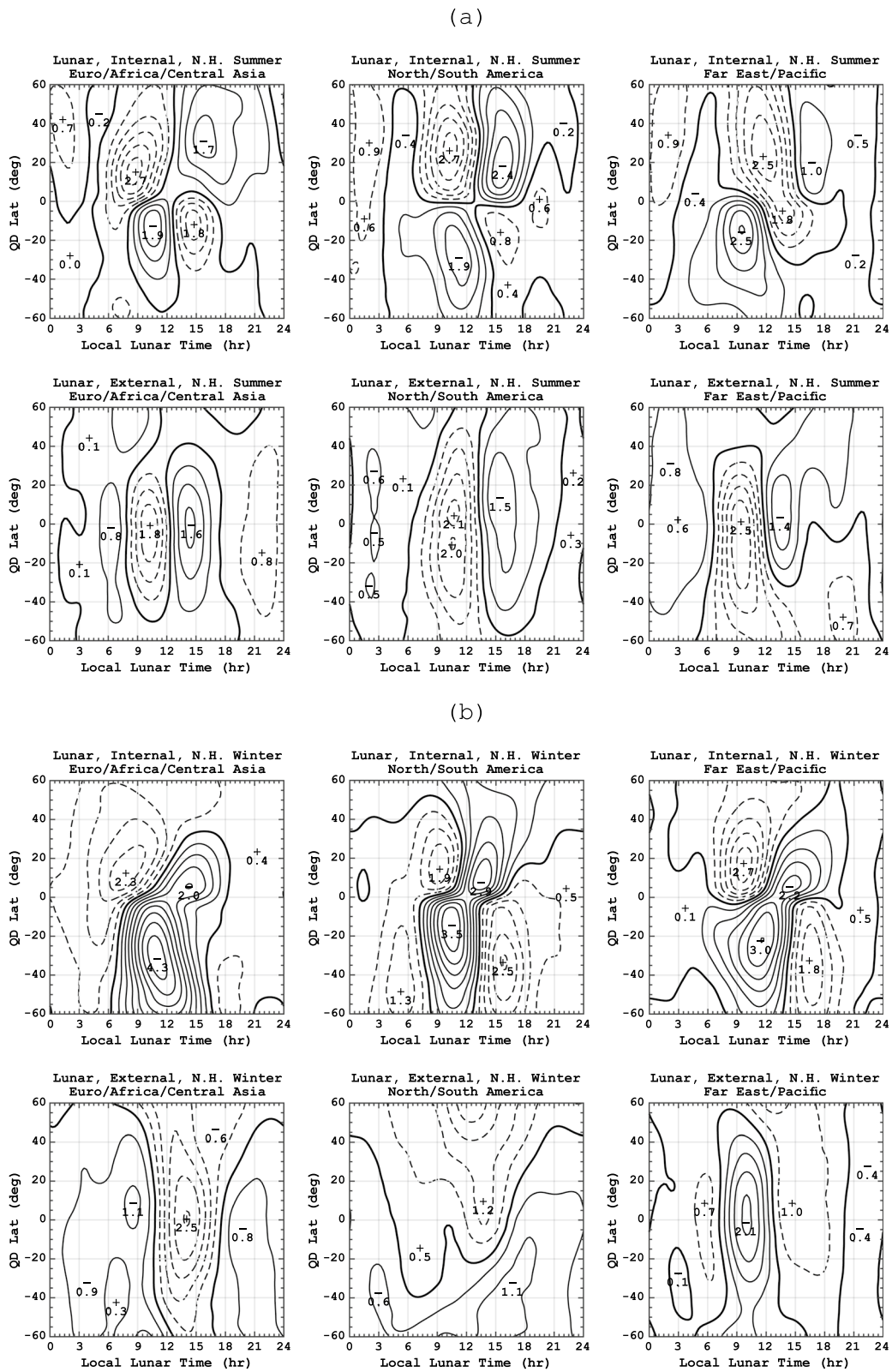**Fig. 8** (See legend on previous page.)

Fig. 9 Same as Fig. 8 except for Swarm equivalent L current systems at the new Moon. Contour steps are 0.5 kA. It is noted that local lunar time equals local solar time at the new Moon.

sector, and a clockwise morning vortex is seen in the Far Eastern/Pacific sector, both of which indicate southward cross-equatorial currents around the noon. In the American sector, on the other hand, the external currents do not exhibit a clear pattern.

Summary and outlook

Using Swarm vector magnetometer data during the solar minimum years of 2017–2020, quiet-time solar (Sq) and lunar (L) daily variations of the geomagnetic field at mid and low latitudes are examined and their equivalent current systems are derived. The evaluation of the Sq and L fields relied on the estimation of the core, crustal and magnetospheric fields by the CHAOS-7 geomagnetic field model (Finlay et al. 2020). In addition, the ocean tidal field was evaluated using the residuals between the nightside Swarm data and corresponding CHAOS-7 predictions, and was removed from the data before analyzing the Sq and L fields. For the first time, both internal and external equivalent current systems of the Sq and L fields are evaluated based on the spherical harmonic analysis of satellite magnetometer data. An important difference from the analysis of ground data is that the Swarm internal and external currents have their sources above and below the height of the satellite ∼500 km, so that the E-region dynamo currents contribute to the internal component. The primary results of this study can be summarized as follows:

- The L field at Swarm altitudes is within approximately ±2 nT in the seasonal and longitudinal mean. This is about one tenth of the Sq field in magnitude, which is within approximately ±14 nT, and is comparable with the ocean tidal field, whose amplitude is less than 2 nT in most areas.
- The Swarm Sq and L fields are primarily of internal origin, which can be attributed to the E-region dynamo currents and induced underground currents.
- The Swarm internal equivalent Sq and L current systems generally show two- and four-dayside-vortex patterns, respectively, which are consistent in pattern with the external current systems previously reported with ground magnetic observations.
- Swarm external Sq and L equivalent current systems often show dayside vortices over the equatorial region, accompanying cross-equatorial meridional currents. The pattern and strength of the external current systems change systematically with season.
- Longitudinal dependence is also found in the Swarm external and internal Sq and L current systems.

The external component of the Swarm Sq field is interpreted as arising from the remote part of interhemispheric field-aligned currents (IHFACs). There is some agreement between the seasonal climatology of IHFACs (Park et al. 2011, 2020a) and the cross-equatorial part of the Swarm external Sq currents. More studies are required to clarify their relationship. The external component of the Swarm L field may also be associated with the lunar variation of IHFACs. However, there is so far little evidence to support this hypothesis, because the lunar variation of IHFACs and its seasonal and longitudinal dependence are not well established.

This study has focused on a solar minimum period. Both Sq and L fields are expected to be greater in magnitude under solar maximum conditions, where the E-region dynamo currents are stronger (Olsen 1993; Çelik 2018). In addition, F-region currents (e.g., Lühr and Maus 2006; Alken et al. 2017) become non-negligible under solar maximum conditions. IHFACs, on the other hand, do not strongly depend on solar activity (Park et al. 2011). It needs to be clarified how these factors affect the Sq and L fields during solar maximum periods.

The longitudinal dependence of Sq and L fields needs to be examined in more detail. The results presented here are based on the separation of the data into three UT groups, thus do not resolve longitudinal structures with zonal wavenumber 2 or more. Previous studies have revealed that longitudinal structures with zonal wavenumber up to 4 or so can be important for the Sq current system (e.g., Pedatella et al. 2011; Chulliat et al. 2016). IHFACs also have longitudinal structures with zonal wavenumber 4–5 (e.g., Park et al. 2020a). For the L current system, the longitudinal structure is less known. The L field in the equatorial electrojet shows longitudinal structures with zonal wavenumber up to 4 (Yamazaki et al. 2017). Resolving these longitudinal structures and their seasonal dependence would require a larger data set.

A larger data set would also allow empirical modeling of the Swarm internal and external Sq and L current systems. Combining the Swarm magnetic data with the measurements from other satellite missions might help achieve this goal. Calibrated magnetic data from non-geomagnetic missions such as CryoSat-2 (Olsen et al. 2020) and GRACE-FO (Stolle et al. 2021) are potentially useful.

References

Alken P (2016) Observations and modeling of the ionospheric gravity and diamagnetic current systems from CHAMP and Swarm measurements. J Geophys Res Space Phys 121:589–601. https://doi.org/10.1002/2015JA022163

Alken P, Maus S (2007) Spatio-temporal characterization of the equatorial electrojet from CHAMP, Ørsted, and SAC-C satellite magnetic measurements. J Geophys Res 112:A09305. https://doi.org/10.1029/2007JA012524

Alken P, Maus S, Chulliat A, Vigneron P, Sirol O, Hulot G (2015) Swarm equatorial electric field chain: first results. Geophys Res Lett 42:673–680. https://doi.org/10.1002/2014GL062658

Alken P, Maute A, Richmond AD (2017) The F F-region gravity and pressure gradient current systems: a review. Space Sci Rev 206(1):451–469

Alken P, Thébault E, Beggan CD, Amit H, Aubert J, Baerenzung J, Bondar TN, Brown W, Califf S, Chambodut A, Chulliat A, Cox G, Finlay CC, Fournier A, Gillet N, Grayver A, Hammer MD, Holschneider M, Huder L, Hulot G, Jager T, Kloss C, Korte M, Kuang W, Kuvshinov A, Langlais B, Léger JM, Lesur V, Livermore PW, Lowes FJ, Macmillan S, Magnes W, Mandea M, Marsal S, Matzka J, Metman MC, Minami T, Morschhauser A, Mound JE, Nair M, Nakano S, Olsen N, Pavón-Carrasco FJ, Petrov VG, Ropp G, Rother M, Sabaka TJ, Sanchez S, Saturnino D, Schnepf NR, Shen X, Stolle C, Tangborn A, Tøffner-Clausen L, Toh H, Torta JM, Varner J, Vervelidou F, Vigneron P, Wardinski I, Wicht J, Woods A, Zeren Z, Yang Y, Zhou B (2021) International geomagnetic reference field: the thirteenth generation. Earth Planets Space 73:49. https://doi.org/10.1186/s40623-020-01288-x

Baldwin MP, Ayarzaguena B, Birner T, Butchart N, Butler AH, Charlton-Perez AJ, Domeisen DIV, Garfinkel CI, Garny H, Gerber EP, Hegglin MI, Langematz U, Pedatella NM (2021) Sudden stratospheric warmings. Rev Geophys. https://doi.org/10.1029/2020RG000708

Campbell WH (1989) The regular geomagnetic-field variations during quiet solar conditions. In: J. A. Jacobs (Ed.), Geomagnetism, Volume 3, 385–460

Campbell WH (1990) Differences in geomagnetic Sq field representations due to variations in spherical harmonic analysis techniques. J Geophys Res Space Phys 95(A12):20923–20936

Campbell WH, Matsushita S (1982) Sq currents: a comparison of quiet and active year behavior. J Geophys Res Space Phys 87(A7):5305–5308

Campbell WH, Schiffmacher ER (1985) Quiet ionospheric currents of the northern hemisphere derived from geomagnetic field records. J Geophys Res Space Phys 90(A7):6475–6486

Campbell WH, Schiffmacher ER (1988) Quiet ionospheric currents of the southern hemisphere derived from geomagnetic records. J Geophys Res Space Phys 93(A2):933–944

Campbell WH, Arora BR, Schiffmacher ER (1993) External Sq currents in the India-Siberia region. J Geophys Res Space Phys 98(A3):3741–3752

Çelik C (2013) The solar daily geomagnetic variation and its dependence on sunspot number. J Atmos Solar Terr Phys 104:75–86

Çelik C (2014) The lunar daily geomagnetic variation and its dependence on sunspot number. J Atmos Solar Terr Phys 119:153–161

Çelik C (2018) Wolf ratios and the ionospheric L and S dynamo region. J Atmos Solar Terr Phys 173:23–27

Chapman S (1951) The equatorial electrojet as detected from the abnormal electric current distribution above Huancayo, Peru, and elsewhere. Archiv Fuer Meteorologie, Geophysik und Bioklimatologie, Serie A 4(1):368–390

Chapman S, Bartels J (1940) Geomagnetism, vol 1. Oxford University Press, Oxford, pp 214–243

Chapman S, Miller JCP (1940) The statistical determination of lunar daily variations in geomagnetic and meteorological elements. Geophys Suppl Monthly Notices Royal Astron Soc 4(9):649–669

Chulliat A, Vigneron P, Hulot G (2016) First results from the Swarm dedicated ionospheric field inversion chain. Earth, Planets and Space 68(1):1–18

Efron B (1981) Nonparametric estimates of standard error: the jackknife, the bootstrap and other methods. Biometrika 68(3):589–599

Emmert JT, Richmond AD, Drob DP (2010) A computationally compact representation of Magnetic-Apex and Quasi!Dipole coordinates with smooth base vectors. J Geophys Res. 115:A08322. https://doi.org/10.1029/2010JA015326

Fejer BG, Olson ME, Chau JL, Stolle C, Lühr H, Goncharenko LP, Yumoto K, Nagatsuma, T. (2010). Lunar-dependent equatorial ionospheric electrodynamic effects during sudden stratospheric warmings. J Geophys Res Space Physics, 115(A8)

Finlay CC, Kloss C, Olsen N, Hammer MD, Tøffner-Clausen L, Grayver A, Kuvshinov A (2020) The CHAOS-7 geomagnetic field model and observed changes in the South Atlantic Anomaly. Earth, Planets and Space 72(1):1–31. https://doi.org/10.1186/s40623-020-01252-9

Forbes JM, Lindzen RS (1976) Atmospheric solar tides and their electrodynamic effects-I. The global Sq current system. J Atmos Terr Phys 38(9–10):897–910

Forbes JM, Zhang X, Palo S, Russell J, Mertens CJ, Mlynczak M (2008) Tidal variability in the ionospheric dynamo region. J Geophys Res Space Phys, 113(A2)

Friis-Christensen E, Lühr H, Hulot G (2006) Swarm: a constellation to study the Earth's magnetic field. Earth, Planets and Space 58(4):351–358. https://doi.org/10.1186/BF03351933.pdf

Friis-Christensen E, Lühr H, Knudsen D, Haagmans R (2008) Swarm-an Earth observation mission investigating geospace. Adv Space Res 41(1):210–216

Fukushima N (1979) Electric potential difference between conjugate points in middle latitudes caused by asymmetric dynamo in the ionosphere. J Geomagn geoelectr 31(3):401–409

Grayver AV, Olsen N (2019) The magnetic signatures of the M 2, N 2, and O 1 oceanic tides observed in Swarm and CHAMP satellite magnetic data. Geophys Res Lett 46(8):4230–4238

Hagan ME, Roble RG, Hackney J (2001) Migrating thermospheric tides. J Geophys Res Space Phys 106(A7):12739–12752

Haines GV, Torta JM (1994) Determination of equivalent current sources from spherical cap harmonic models of geomagnetic field variations. Geophys J Int 118(3):499–514

Heelis RA (2004) Electrodynamics in the low and middle latitude ionosphere: a tutorial. J Atmos Solar Terr Phys 66(10):825–838

Koch S, Kuvshinov A (2013) Global 3-D EM inversion of Sq variations based on simultaneous source and conductivity determination: concept validation and resolution studies. Geophys J Int 195(1):98–116

Koch S, Kuvshinov A (2015) 3-D EM inversion of ground based geomagnetic Sq data. Results from the analysis of Australian array (AWAGS) data. Geophys J Int 200(3):1284–1296

Kuvshinov A, Manoj C, Olsen N, Sabaka T (2007) On induction effects of geomagnetic daily variations from equatorial electrojet and solar quiet sources at low and middle latitudes. J Geophys Res Solid Earth 112:B10102

Kuvshinov A, Grayver A, Tøffner-Clausen L, Olsen N (2021) Probing 3-D electrical conductivity of the mantle using 6 years of Swarm, CryoSat-2 and observatory magnetic data and exploiting matrix Q-responses approach. Earth, Planets and Space 73(1):1–26. https://doi.org/10.1186/s40623-020-01341-9

Laundal KM, Richmond AD (2017) Magnetic coordinate systems. Space Sci Rev 206(1):27–59

Laundal KM, Finlay CC, Olsen N, Reistad JP (2018) Solar wind and seasonal influence on ionospheric currents from Swarm and CHAMP measurements. J Geophys Res Space Physics 123(5):4402–4429

Leger JM, Bertrand F, Jager T, Le Prado M, Fratter I, Lalaurie JC (2009) Swarm absolute scalar and vector magnetometer based on helium 4 optical pumping. Procedia Chem 1(1):634–637

Le Sager P, Huang TS (2002) Ionospheric currents and field-aligned currents generated by dynamo action in an asymmetric Earth magnetic field. J Geophys Res Space Phys 107(A2):SIA-4

Lindzen RS, Chapman S (1969) Atmospheric tides. Space Sci Rev 10(1):3–188

Lühr H, Maus S (2006) Direct observation of the F region dynamo currents and the spatial structure of the EEJ by CHAMP. Geophysical research letters, 33(24)

Lühr H, Rother M, Maus S, Mai W, Cooke D (2003) The diamagnetic effect of the equatorial Appleton anomaly: Its characteristics and impact on geomagnetic field modeling. Geophysical Research Letters, 30(17)

Lühr H, Maus S, Rother M (2004) Noon-time equatorial electrojet: Its spatial features as determined by the CHAMP satellite. J Geophys Res Space Phys. 109(A1)

Lühr H, Kervalishvili G, Michaelis I, Rauberg J, Ritter P, Park J, Merayo JMG, Brauer P (2015) The interhemispheric and F region dynamo currents revisited with the Swarm constellation. Geophys Res Lett 42(9):3069–3075

Lühr H, Xiong C, Olsen N, Le G (2017) Near-Earth magnetic field effects of large-scale magnetospheric currents. Space Sci Rev 206(1):521–545

Lühr H, Kervalishvili GN, Stolle C, Rauberg J, Michaelis I (2019) Average characteristics of low-latitude interhemispheric and F region dynamo currents deduced from the swarm satellite constellation. J Geophys Res Space Phys 124(12):10631–10644

Malin SRC (1970) Separation of lunar daily geomagnetic variations into parts of ionospheric and oceanic origin. Geophys J Int 21(5):447–455

Malin SR (1973) Worldwide distribution of geomagnetic tides. Philos Trans Royal Soc London. 274(1243):551–594

Matsushita S (1968) Sq and L current systems in the ionosphere. Geophys J Int 15(1–2):109–125

Matsushita S, Maeda H (1965a) On the geomagnetic solar quiet daily variation field during the IGY. J Geophys Res 70(11):2535–2558

Matsushita S, Maeda H (1965b) On the geomagnetic lunar daily variation field. J Geophys Res 70(11):2559–2578

Matsushita S, Xu WY (1984) Seasonal variations of L equivalent current systems. J Geophys Res Space Phys 89(A1):285–294

Matzka J, Stolle C, Yamazaki Y, Bronkalla O, Morschhauser A (2021) The geomagnetic Kp index and derived indices of geomagnetic activity. Space Weather, 19(5):e2020SW002641

Matzka J, Bronkalla O, Kervalishvili G, Rauberg J, Yamazaki Y (2022) Geomagnetic Hpo index. V. 2.0. GFZ Data Services. https://doi.org/10.5880/Hpo.0002

Maus S, Rother M, Hemant K, Stolle C, Lühr H, Kuvshinov A, Olsen N (2006) Earth's lithospheric magnetic field determined to spherical harmonic degree 90 from CHAMP satellite measurements. Geophys J Int 164(2):319–30

Maus S, Lühr H (2006) A gravity-driven electric current in the Earth's ionosphere identified in CHAMP satellite magnetic measurements. Geophys Res Lett. 33(2)

Maute A, Richmond AD (2017) *F*-region dynamo simulations at low and mid-latitude. Space Sci Rev 206(1):471–493

Miyahara S, Ooishi M (1997) Variation of Sq induced by atmospheric tides simulated by a middle atmosphere general circulation model. J Geomagn Geoelectr. 49(1):77–87

Oberheide J, Pedatella NM, Gan Q, Kumari K, Burns AG, Eastes RW (2020) Thermospheric composition O/N response to an altered meridional mean circulation during sudden stratospheric warmings observed by GOLD. Geophys Res Lett. 47(1):e2019GL086313

Olsen N (1993) The solar cycle variability of lunar and solar daily geomagnetic variations. Annales Geophysicae 11(4):254–262

Olsen N (1997) Ionospheric F region currents at middle and low latitudes estimated from Magsat data. J Geophys Res Space Phys 102(A3):4563–4576

Olsen N, Stolle C (2012) Satellite geomagnetism. Annu Rev Earth Planet Sci 40:441–465

Olsen N, Albini G, Bouffard J, Parrinello T, Tøffner-Clausen L (2020) Magnetic observations from CryoSat-2: calibration and processing of satellite platform magnetometer data. Earth, Planets and Space 72(1):1–18. https://doi.org/10.1186/s40623-020-01171-9

Owolabi C, Ruan H, Yamazaki Y, Kaka RO, Akinola, OO, Yoshikawa A (2022) Ionospheric current variations by empirical orthogonal function analysis: solar activity dependence and longitudinal differences. J Geophys Res Space Phys, 127(1):e2021JA029903

Park J, Lühr H, Min KW (2010) Characteristics of F-region dynamo currents deduced from CHAMP magnetic field measurements. J Geophys Res Space Phys. 115(A10)

Park J, Lühr H, Min K (2011) Climatology of the inter-hemispheric field-aligned current system in the equatorial ionosphere as observed by CHAMP. Annales Geophysicae 29(3):573–582

Park J, Yamazaki Y, Lühr H (2020a) Latitude dependence of Interhemispheric Field-Aligned Currents (IHFACs) as observed by the Swarm constellation. J Geophys Res Space Phys, 125(2):e2019JA027694

Park J, Stolle C, Yamazaki Y, Rauberg J, Michaelis I, Olsen N (2020) Diagnosing low-/mid-latitude ionospheric currents using platform magnetometers: CryoSat-2 and GRACE-FO. Earth, Planets and Space 72(1):1–18

Paulino AR, Batista PP, Batista IS (2013) A global view of the atmospheric lunar semidiurnal tide. J Geophys Res Atmos 118(23):13–128

Pedatella NM (2014) Observations and simulations of the ionospheric lunar tide: seasonal variability. J Geophys Res Space Phys 119(7):5800–5806

Pedatella NM, Forbes JM, Richmond AD (2011) Seasonal and longitudinal variations of the solar quiet (Sq) current system during solar minimum determined by CHAMP satellite magnetic field observations. Journal of Geophysical Research: Space Physics, 116(A4)

Pedatella NM, Liu HL, Richmond AD (2012a) Atmospheric semidiurnal lunar tide climatology simulated by the Whole Atmosphere Community Climate Model. Journal of Geophysical Research: Space Physics, 117(A6)

Pedatella NM, Liu HL, Richmond AD, Maute A, Fang TW (2012b) Simulations of solar and lunar tidal variability in the mesosphere and lower thermosphere during sudden stratosphere warmings and their influence on the low-latitude ionosphere. J Geophys Res Space Phys. 117(A8)

Pfaff R, Larsen M, Abe T, Habu H, Clemmons J, Freudenreich H, Rowland D, Bullett T, Yamamoto MY, Watanabe S, Kakinami Y, Yokoyama T, Mabie J, Klenzing J, Bishop R, Walterscheid R, Yamamoto M, Yamazaki Y, Murphy N, Angelopoulos V (2020) Daytime dynamo electrodynamics with spiral currents driven by strong winds revealed by vapor trails and sounding rocket probes. Geophys Res Lett. 47(15):e2020GL088803

Rao J, Ren R, Chen H, Yu Y, Zhou Y (2018) The stratospheric sudden warming event in February 2018 and its prediction by a climate system model. J Geophys Res Atmos 123(23):13–332

Rastogi RG, Trivedi NB (1970) Luni-solar tides in H at stations within the equatorial electrojet. Planet Space Sci. 18(3):367–77

Reigber C, Lühr H, Schwintzer P (2002) CHAMP mission status. Adv Space Res 30(2):129–134

Richmond AD (1995) Ionospheric electrodynamics. In: Volland H (ed) Handbook of atmospheric electrodynamics, vol 2. CRC Press, Boca Raton, pp 249–290

Richmond AD (1995) Ionospheric electrodynamics using magnetic apex coordinates. J Geomagn Geoelectr 47(2):191–212

Richmond AD (2011) Electrodynamics of ionosphere-thermosphere coupling. In: Abdu MA, Pancheva D (eds) Aeronomy of the Earth's atmosphere and ionosphere. Springer, Dordrecht, pp 191–201

Richmond AD, Roble RG (1987) Electrodynamic effects of thermospheric winds from the NCAR thermospheric general circulation model. J Geophys Res Space Phys 92(A11):12365–12376

Richmond AD, Matsushita S, Tarpley JD (1976) On the production mechanism of electric currents and fields in the ionosphere. J Geophys Res 81(4):547–555

Rishbeth H (1981) The F-region dynamo. J Atmos Terr Phys. 43(5–6):387–92

Rodríguez-Zuluaga J, Stolle C (2019) Interhemispheric field-aligned currents at the edges of equatorial plasma depletions. Sci Rep 9(1):1–8

Sabaka TJ, Olsen N, Langel RA (2002) A comprehensive model of the quiet-time, near-Earth magnetic field: phase 3. Geophys J Int 151(1):32–68

Sabaka TJ, Tøffner-Clausen L, Olsen N, Finlay CC (2018) A comprehensive model of Earth's magnetic field determined from 4 years of Swarm satellite observations. Earth, Planets and Space 70(1):1–26. https://doi.org/10.1186/s40623-018-0896-3

Saynisch-Wagner J, Baerenzung J, Hornschild A, Irrgang C, Thomas M (2021) Tide-induced magnetic signals and their errors derived from CHAMP and Swarm satellite magnetometer observations. Earth, Planets and Space 73(1):1–11. https://doi.org/10.1186/s40623-021-01557-3

Schnepf NR, Manoj C, Kuvshinov A, Toh H, Maus S (2014) Tidal signals in ocean-bottom magnetic measurements of the Northwestern Pacific: observation versus prediction. Geophys J Int 198(2):1096–1110

Stening RJ (1971) Longitude and seasonal variations of the Sq current system. Radio Sci 6(2):133–137

Stening RJ (1995) What drives the equatorial electrojet? J Atmos Terr Phys 57(10):1117–1128

Stening RJ, Winch DE (1979) Seasonal changes in the global lunar geomagnetic variation. J Atmos Terr Phys 41(3):311–323

Stening RJ, Winch DE (2013) The ionospheric Sq current system obtained by spherical harmonic analysis. J Geophys Res Space Phys 118(3):1288–1297

Stening RJ, Forbes JM, Hagan ME, Richmond AD (1997) Experiments with a lunar atmospheric tidal model. J Geophys Res Atmos 102(D12):13465–13471

Stolle C, Michaelis I, Rauberg J (2016) The role of high-resolution geomagnetic field models for investigating ionospheric currents at low Earth orbit satellites. Earth, Planets and Space 68(1):1–10. https://doi.org/10.1186/s40623-016-0494-1

Stolle C, Michaelis I, Xiong C, Rother M, Usbeck T, Yamazaki Y, Rauberg J, Styp-Rekowski K (2021) Observing Earth's magnetic environment with the GRACE-FO mission. Earth, Planets and Space 73(1):1–21. https://doi.org/10.1186/s40623-021-01364-w

Sugiura M, Fanselau G (1966) Lunar phase numbers ν and ν′ for years 1850 to 2050 (U.S. NASA Goddard Space Flight Center, Report X-612-66-401)

Takeda M (1990) Geomagnetic field variation and the equivalent current system generated by an ionospheric dynamo at the solstice. J Atmos Terr Phys 52(1):59–67

Takeda M (1999) Time variation of global geomagnetic Sq field in 1964 and 1980. J Atmos Solar Terr Phys 61(10):765–774

Takeda M (2002) Features of global geomagnetic Sq field from 1980 to 1990. J Geophys Res Space Phys 107(A9):SIA-4

Takeda M, Maeda H (1980) Three-dimensional structure of ionospheric currents 1. Currents caused by diurnal tidal winds. J Geophys Res Space Phys 85(A12):6895–6899

Tapping KF (2013) The 10.7 cm solar radio flux (F10.7). Space Weather 11(7):394–406

Tarpley JD (1970) The ionospheric wind dynamo-I: Lunar tide. Planet Space Sci 18(7):1075–1090

Thébault E, Vigneron P, Langlais B, Hulot G (2016) A Swarm lithospheric magnetic field model to SH degree 80. Earth, Planets and Space 68(1):1–13. https://doi.org/10.1186/s40623-016-0510-5

Turner J, Winch D, Ivers D, Stening R (2005) Analysis of satellite magnetic data. Explor Geophys 36(3):317–321

Turner JPR, Winch DE, Ivers DJ, Stening RJ (2007) Regular daily variations in satellite magnetic total intensity data. Annales Geophysicae 25(10):2167–2174

Tyler RH, Maus S, Luhr H (2003) Satellite observations of magnetic fields due to ocean tidal flow. Science 299(5604):239–241

van Sabben D (1966) Magnetospheric currents, associated with the NS asymmetry of Sq. J Atmos Terr Phys 28(10):965–982

Vial F, Forbes JM (1994) Monthly simulations of the lunar semi-diurnal tide. J Atmos Terr Phys 56(12):1591–1607

Wagner CU, Möhlmann D, Schäfer K, Mishin VM, Matveev MI (1980) Large-scale electric fields and currents and related geomagnetic variations in the quiet plasmasphere. Space Sci Rev 26(4):391–446

Xiong C, Lühr H, Wang H, Johnsen MG (2014) Determining the boundaries of the auroral oval from CHAMP field-aligned current signatures-Part 1. Annales Geophysicae 32(6):609–622

Yamashita S, Iyemori T (2002) Seasonal and local time dependences of the interhemispheric field-aligned currents deduced from the Ørsted satellite and the ground geomagnetic observations. J Geophys Res Space Phys, 107(A11):SIA-11

Yamazaki Y (2014) Solar and lunar ionospheric electrodynamic effects during stratospheric sudden warmings. J Atmos Solar Terr Phys 119:138–146

Yamazaki Y, Maute A (2017) Sq and EEJ-A review on the daily variation of the geomagnetic field caused by ionospheric dynamo currents. Space Sci Rev 206(1):299–405. https://doi.org/10.1007/s11214-016-0282-z

Yamazaki Y, Yumoto K, Cardinal MG, Fraser BJ, Hattori P, Kakinami Y, Liu JY, Lynn KJW, Marshall R, McNamara D, Nagatsuma T, Nikiforov VM, Otadoy RE, Ruhimat M, Shevtsov BM, Shiokawa K, Abe S, Uozumi T, Yoshikawa A (2011) An empirical model of the quiet daily geomagnetic field variation. J Geophys Res. 116:A10312. https://doi.org/10.1029/2011JA016487

Yamazaki Y, Richmond AD, Maute A, Wu Q, Ortland DA, Yoshikawa A, Adimula IA, Rabiu B, Kunitake M, Tsugawa T (2014) Ground magnetic effects of the equatorial electrojet simulated by the TIE-GCM driven by TIMED satellite data. J Geophys Res Space Phys. https://doi.org/10.1002/2013JA019487

Yamazaki Y, Stolle C, Matzka J, Siddiqui TA, Lühr H, Alken P (2017) Longitudinal variation of the lunar tide in the equatorial electrojet. J Geophys Res Space Phys 122(12):12–445

Yamazaki Y, Stolle C, Siddiqui T, Laštovička J, Mošna Z, Kozubek M, Ward W, Themens DR, Kristoffersen S (2020) VERA: VERtical coupling in Earth's Atmosphere at mid and high latitudes – Final Report, Potsdam, German Research Centre for Geosciences GFZ, pp 138, https://doi.org/10.2312/GFZ.2.3.2020.001

Yamazaki Y, Matzka J, Stolle C, Kervalishvili G, Rauberg J, Bronkalla O, Morschhauser A, Bruinsma S, Shprits YY, Jackson DR (2022) Geomagnetic activity index Hpo, Geophys Res Lett 49:e2022GL098860. https://doi.org/10.1029/2022GL098860

Zhang JT, Forbes JM (2013) Lunar tidal winds between 80 and 110 km from UARS/HRDI wind measurements. J Geophys Rese Space Phys 118(8):5296–5304

Zhang X, Forbes JM (2014) Lunar tide in the thermosphere and weakening of the northern polar vortex. Geophys Res Lett 41(23):8201–8207

Publisher's Note